Editors' Suggestion

Observation of double-kink states in multivalley acoustic crystals

Xiao-Hui Gou,[1,2] Hua-Shan Lai,[1] Xiao-Chen Sun,[1,3,*] Si-Yuan Yu,[1,3,4] Y. B. Chen,[2] Cheng He,[1,3,4,†] and Yan-Feng Chen[1,3,4,‡]

[1]*National Laboratory of Solid State Microstructures & Department of Materials Science and Engineering, Nanjing University, Nanjing 210093, China*

[2]*School of Physics, Nanjing University, Nanjing 210093, China*

[3]*Collaborative Innovation Center of Advanced Microstructures, Nanjing University, Nanjing 210093, China*

[4]*Jiangsu Key Laboratory of Artificial Functional Materials, Nanjing University, Nanjing 210093, China*

(Received 29 August 2023; revised 6 December 2023; accepted 25 January 2024; published 15 February 2024)

The Dirac degeneracy of band structures, along with the valley states after breaking, holds promising potential for robust signal processing. However, the conventional graphene structure only harbors a single pair of Dirac points, limiting its capacity for information storage and manipulation, and hindering its application in small-sized on-chip devices. In this study, we experimentally investigate S-graphene acoustic crystals that host two pairs of Dirac points and valleys. By examining the interplay between these multivalley pairs, we observe double-kink edge states that display *W*-type and *M*-type dispersions self-guiding at zigzag- and bearded boundaries in a single sample, respectively, eliminating the requirement of a cladding layer in conventional valley Hall effect. Additionally, benefiting from the increased degree of freedom, a superdirectional yet adjustable topological antenna is demonstrated by selectively exciting a specific valley branch. This research expands the degree of freedom for valleytronics and has the potential to stimulate the exploration of multiple spin-valley couplings and the design of unique functional devices.

DOI: 10.1103/PhysRevB.109.054109

I. INTRODUCTION

In the past few decades, two-dimensional (2D) graphene and graphenelike materials have gained considerable attention due to their unique Dirac point (DP) in their band structures. DP is the linear intersection between the conduction- and valence bands, and near such a singularity point in momentum space, many intriguing phenomena have been observed. These include Klein tunneling [1] and Zitterbewegung [2], which were proposed nearly a century ago and have recently been observed in photonic and acoustic metamaterials with similar Dirac band structures [3–5]. Moreover, recent studies of Dirac physics from the topological point of view have significantly advanced the subject, leading to the emergence of a wide field of research, including but not limited to topological semimetals and topological insulators. For example, one can always find one-dimensional edge states formatting arc dispersion connected to bulk DPs [6–8]. Lifting the degeneracy to open band gaps via breaking time-reversal symmetry, spatial-inversion symmetry, or enforcing spin-orbit coupling would give rise to quantum Hall [9–12], valley Hall [13–16], or quantum spin Hall effects [17–20], respectively. These topologically protected edge states enrich the degree of freedom (DOF) for wave manipulation, opening up new applications by exploiting defect-immune and robust signal transport.

In particular, the valley DOF, characterized by a local extremum of energy band that can be used to store and carry information, is highly favored due to its reliance solely on the breaking of inversion symmetry [21], thereby reducing experimental complexity. One hallmark feature is the valley-kink state located at the domain wall between two crystals with opposite valley Chern numbers [15,16,22–24]. Since the intervalley scattering can be largely suppressed, the topological valley propagation is robust against sharp bends. These novel properties, e.g., the valley-dependent vortex and valley-momentum locking, lead to valleytronics [25] and show great potential in practical applications such as valley filters [26,27] and topological antennas [28,29]. The recent combination of valleys with the layer or spin DOF represents a significant step forward in exploiting valley topology. Several kinds of bilayer-valley [30] and spin-valley coupled states [31] have been experimentally demonstrated.

However, previous studies in the realm of 2D acoustic models have primarily focused on a single pair of valleys [14,15,24,29], often necessitating an additional cladding layer to provide valley DOFs, a requirement that inevitably impacts the compactness of valley devices. Valleys coupled to the layer or spin inevitably resort to the out-of-plane dimension [30,31], which is challenging and unfriendly for on-chip devices. To date, creating and broadening additional in-plane DOFs remains an open question, and the behaviors of multiple paired valleys and their interplay are still elusive. Furthermore, the implications of having a sufficient number of in-plan DOFs on valley devices remain largely unknown. Resembling large Chern number cases in magnetic systems [32,33], the realization of multivalleys will undoubtedly increase the number and capacity of topological channels, thus deserving

*Corresponding author: xcsun@nju.edu.cn
†Corresponding author: chenghe@nju.edu.cn
‡Corresponding author: yfchen@nju.edu.cn

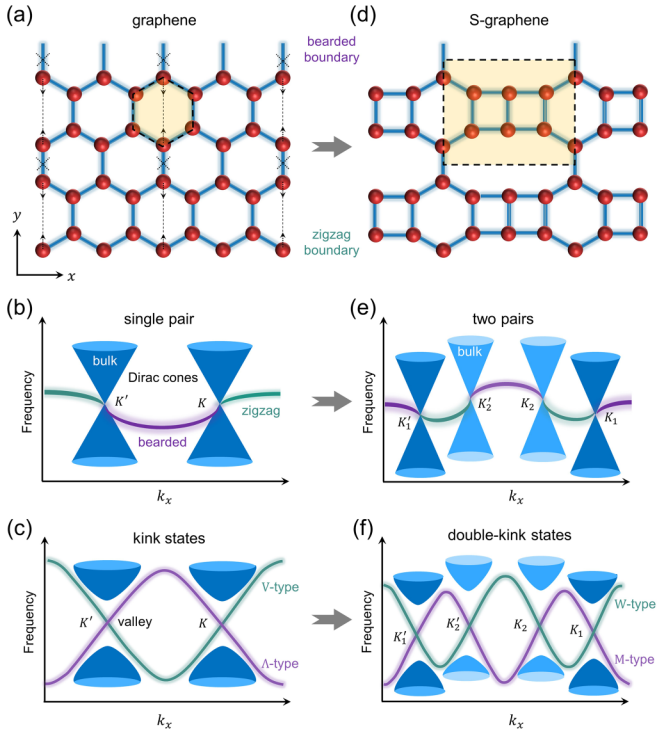

FIG. 1. From graphene to *S*-graphene. (a) Graphene structure with lower-zigzag and upper-bearded boundaries. (b) Schematic of band structures for graphene, containing a pair of DPs (K/K') associated with edge arcs. (c) Single-kink states in a conventional valley system. (d) S-graphene structure by reconstructing several neighboring graphene bonds, marked as crosses and arrows in (a). The shaded area represents a primary unit cell. (e) Band structures for *S*-graphene, containing two pairs of DPs (K_1/K_1' and K_2/K_2') associated with segmental edge arcs. (f) Double-kink states in multivalley acoustic crystals.

detailed investigation. Similar to various Fermi arcs in three-dimensional topological semimetals with exotic topological charges [34,35], a multi-DP system in 2D may also introduce new valley types yet to be explored.

Back to a typical 2D graphene structure, there are two inequivalent atoms in a unit cell, enabling a pair of twofold Dirac degeneracy at the corners of honeycomb Brillouin zone (BZ), i.e., K and K' points, guaranteed by time-reversal and lattice symmetries. Due to bulk-boundary correspondence characterized by quantized Berry phase, the connection fashion of the edge arcs depends on certain boundary conditions [8]. The edge arc crosses the Brillouin boundary or center, corresponding to zigzag or bearded boundaries. After breaking spatial symmetry, the kink states exhibit conventional V-type and Λ-type dispersions at different domain walls accordingly [15,16], as shown in Figs. 1(a)–1(c). But, for the *S*-graphene structure [36], which is a Dirac carbon allotrope of graphene via reconstructing several neighboring C–C bonds, the unit cell becomes rectangular and contains eight atoms [Fig. 1(d)]. It can accommodate two pairs of DPs in the band structure, denoted as K_1/K_1' and K_2/K_2'. Each edge arc splits into two segments, unlike one Dirac pair case. Both intrapair and interpair connections are possible [Fig. 1(e)]. Consequently, there are four valleys in the first BZ after breaking the spatial symmetry, whose associated valley states are in double-kink fashions [W type and M type shown in Fig. 1(f)] self-guiding on the different boundaries, which significantly reduces the size and improves the compactness of the device.

In this work, we focus on the experimental demonstration of double-kink states in multivalley acoustic crystals with *S*-graphene structures. Owing to the interaction of different valley pairs, this valley state can be supported at the boundary of a single crystal without the need for an opposite valley crystal as a cladding. By utilizing symmetry or antisymmetry phase arrays of two sources, we can select one particular branch of the double-kink valley state to achieve superdirectional yet tunable topological antennas. Our results further extend the valley DOF and shed light on the exploration of multiplexing functions of multivalley devices.

II. RESULTS

A. Acoustic structure of *S*-graphene and its four DPs

Herein, our acoustic crystal is composed of air cavities and connecting tubes, which act as acoustic atoms and couplings. As shown in Fig. 2(a), the unit cell is rectangular with lattice constants $a_x = (2+\sqrt{3})a$ and $a_y = 3a$, where $a = 6$ mm is the site spacing. The radius of circular cavities (r) and the width of coupling tubes (t) are set to $0.4a$. There are two pairs of DPs, denoted as K_1/K_1' and K_2/K_2', located at the high-symmetry lines ΓX ($k_y = 0$) and MY ($k_y = \pi/a_y$) directions in the first BZ. The numerical bulk band structures are plotted in Fig. 2(b), showing that the frequencies of all DPs are close to 16 kHz in this case. In calculations, we choose the velocity (density) of the air to be 345 m/s (1.25 kg/m^3). Note in a time-reversal symmetry-invariant system, each pair of DPs has the same frequency. However, the frequency of different pairs could differ, in this case, a slightly lower frequency for K_1/K_1'. This is because the K_1/K_1' DP comes from the crossing of the fourth and fifth bands, while the K_2/K_2' is of the third and sixth bands (see Appendix A); they are different types of DPs and their robustness is protected within a certain parameter space [37]. It means that for different pairs, we can independently control not only the Dirac frequencies but also the positions in the momentum space along the ΓX or MY direction, benefiting further manipulations.

In experiments, we fabricate the *S*-graphene acoustic crystal with a full dimension of $26a_x \times 11a_y$ [Fig. 2(c)]. The plate height is 5 mm, ensuring it can act as a 2D model covering the frequency of interest. The lower and upper boundaries (along the x axis) are set to typical zigzag and bearded boundaries as in conventional graphene cases. A little decoration is performed for experimental convenience to distinguish the edge arcs from the bulk bands. In Fig. 2(d), we measure transmission spectra for the bulk (blue line), zigzag boundary (cyan line), and bearded boundary (purple line), respectively. They remain at high values from 15.5 to 16.5 kHz, indicating the gapless behavior for both bulk and edge states. A slight dip in the bulk transmission is due to the pseudodiffusion behavior near Dirac frequencies [5,38,39].

To study the bulk-boundary correspondence of our multi-DP system, we resort to Berry phases of bulk to characterize edge arcs. Generally, the unit cell chosen for the Berry phase calculation should be centrosymmetric to get a quantized value of 0 or π. But, the unit cells with a zigzag- or bearded-

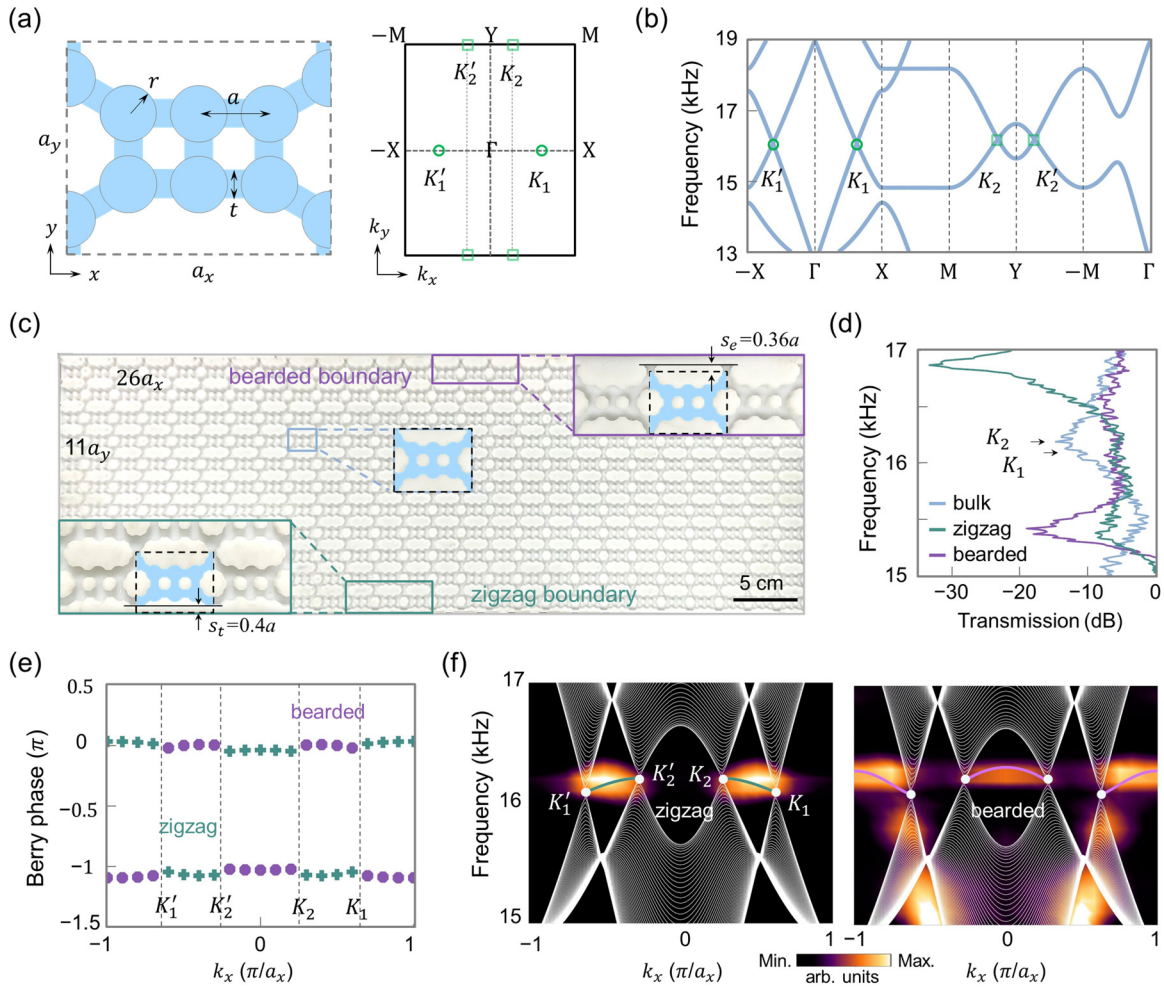

FIG. 2. Acoustic *S*-graphene with multiple DPs. (a) A unit cell and the first BZ. Sound propagates in the shaded area. The geometrical parameters are $a = 6$ mm and $r = t = 0.4a$. Circular (rectangular) markers denote a pair of K_1/K_1' (K_2/K_2') DPs. (b) Bulk-band structures along high-symmetry directions. (c) Picture of the acoustic sample with 26 × 11 periods. The lower (upper) boundary belongs to the zigzag (bearded) type with truncated (elongated) length $s_t = 0.4a$ ($s_e = 0.36a$). The insets show magnified structures. (d) Measured transmission spectra for the bulk (blue line), zigzag (cyan line), and bearded boundary (purple line). (e) Berry phases for the zigzag (cyan dots) and bearded (purple dots) boundaries. (f) Measured edge arcs (color scale) and calculated arcs (cyan and purple lines) connecting to DPs. The color scale represents the strength of the acoustic energy density with arbitrary units (arb. units). The white lines are numerical bulk states.

boundary morphology selected here are asymmetric since the boundaries are decorated. Here, we use relative Berry phases to characterize the existence of edge states with noncentrosymmetric unit cells (see Appendix B). Via Wilson loop to calculate, the Berry phases Φ for every fixed k_x [40,41] can be divided into two categories, e.g., Φ_1 between the projection of the same Dirac pair ($K_1 - K_1'$ and $K_2 - K_2'$) and Φ_2 between the projection of different Dirac pair ($K_1 - K_2$ and $K_1' - K_2'$). Their difference satisfies

$$|\Phi_1 - \Phi_2| \approx \pi. \tag{1}$$

It is worth noting that the original calculated values are not equal to the standard values 0 or $-\pi$ [see Figs. 6(b) and 6(e)]. However, it can be shifted down by the same average value to approximately meet the standard values, which is our relative Berry phase (Φ^r). As shown in Fig. 2(e), for the bearded boundary ($\Phi^r = \Phi - \bar{\Phi}_2$), the relative Berry phases are quantized to approximately $-\pi$ between the $K_1 - K_1'$ (and equivalent $K_2 - K_2'$), while they are zero in the other region. On the contrary, for the zigzag case, the $-\pi$ relative Berry phases appear between different Dirac pairs, implying edge arcs.

We further experimentally measure these edge arcs via Fourier transforming the scanned acoustic pressures of 25 periodic cavities. The edge arcs observed in Fig. 2(f) are clear evidence for the bulk-boundary correspondence of multi-Dirac acoustic crystals. The edge arcs for zigzag and bearded boundaries appear in complementary momentum regions. Generally, an arbitrary boundary in our two-pair DP system exhibits two segmental arcs (see Appendix C). Both intra- and interpair connections are allowed. More segmental arcs can be expected with more DPs.

B. The double-kink edge states

Multiple DPs will also give rise to multivalley DOFs. Here, we break the spatial-inversion symmetry, using two

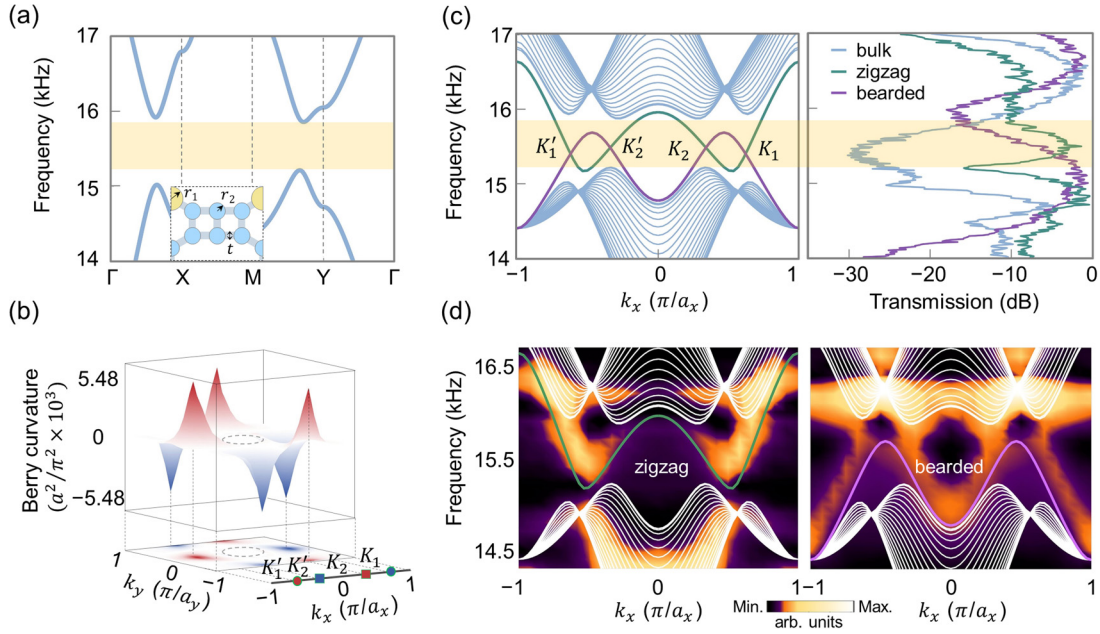

FIG. 3. Acoustic double-kink valley states. (a) The bulk-band structures with broken spatial-inversion symmetry. The inset shows the unit cell with parameters $r_1 = 0.47a$, $r_2 = 0.33a$, and $t = 0.3a$. The shaded region indicates the full band gap. (b) The calculated Berry curvature of the band below the gap, excluding the region near the BZ center. (c) Left panel: the projected band structure, where the cyan line (purple line) represents the *W*-type (*M*-type) double-kink states at the zigzag (bearded) boundary. Right panel: the experimental transmission spectra for the bulk (blue line), zigzag (cyan line), and bearded boundaries (purple line), respectively. (d) Experimentally measured double-kink valley states (color scale). The white lines are the numerical bulk states.

distinct sets of cavities with $r_1 = 0.47a$ and $r_2 = 0.33a$, to lift Dirac degeneracies. The connecting tubes are finely tuned ($t = 0.3a$) to ensure a full band gap, which ranges from 15.21 to 15.91 kHz, as shown in Fig. 3(a). We calculate the Berry curvature around each valley for the lower band excluding the BZ center (see Appendix D) and then project it onto the k_x axis [Fig. 3(b)]. The valleys K_1' and K_2 are positive while the valleys K_2' and K_1 are negative. Interestingly, the valleys born from different DP pairs get opposite signs, indicating the opposite chirality (see Appendix E). Considering that each valley gets $\pm 1/2$ valley Chern number (C_v) after DP breaking, we can align the C_v for four valleys with increasing wave vectors,

$$C_v^{K_1'} = +1/2,\ C_v^{K_2'} = -1/2,\ C_v^{K_2} = +1/2,\ C_v^{K_1} = -1/2. \tag{2}$$

For example, the K_1' valley and its neighboring but opposite K_2' valley, both located at the negative half region of the BZ, would couple with each other to produce ± 1 difference in C_v. Thus, unlike conventional valley states at the domain wall between two opposite valley crystals, this multivalley acoustic crystal itself could support *V*-type or Λ-type valley states (depending on the sign) in a half BZ. After adding its time-reversal-symmetry partner, the resulting valley edge states kink twice to form the *W*-type or *M*-type dispersions.

We then calculate the projected band structure and experimentally measure transmission spectra for the bulk, zigzag, and bearded boundaries, respectively [Fig. 3(c)]. The high transmission along the boundary confirms the existence of valley edge states. We also perform the acoustic field-scanning measurement to map double-kink states in Fig. 3(d), which is in good agreement with the numerical calculations. In this case, both the zigzag and bearded boundary conditions are chosen to be hard boundaries without the need for additional decorations [42–44] or a cladding crystal (see Appendix F). Hence, the self-guiding valley states can be generated at each of the two boundaries merely by changing the radius of the circular cavity (see Appendix G). The *W*-type or *M*-type dispersion based on the zigzag or bearded boundary in the multivalley crystal can be treated as the topological hierarchy from different edge arcs of the multi-DP crystal. Compared with the conventional domain-wall configuration, our double-kink valley state is supported on its own boundary in a more compact device.

C. The superdirectional sound radiation of double-kink valley states

The unique double-kink states increase the valley DOF, which is promising for many applications, such as the directional yet tunable sound biradiation. Here, we focus on the *W*-type valley state at the zigzag boundary, and a similar analysis can be applied to the valley state at the bearded boundary. The double-kink states can provide more topological channels. For the case of forward propagation (along the $+x$ axis) at a frequency of 15.4 kHz, there are two branches (with positive group velocities), marked as symmetrical (S) and antisymmetrical (AS) modes corresponding to K_1 and K_2' valleys, respectively (see Appendix H). In order to couple the valley state to air in a *y*-cut sample, the wave vectors along the tangential direction (*y* axis) should be conserved. As shown in Fig. 4(a), if we choose to excite the S branch, only $k_y = 0$ is

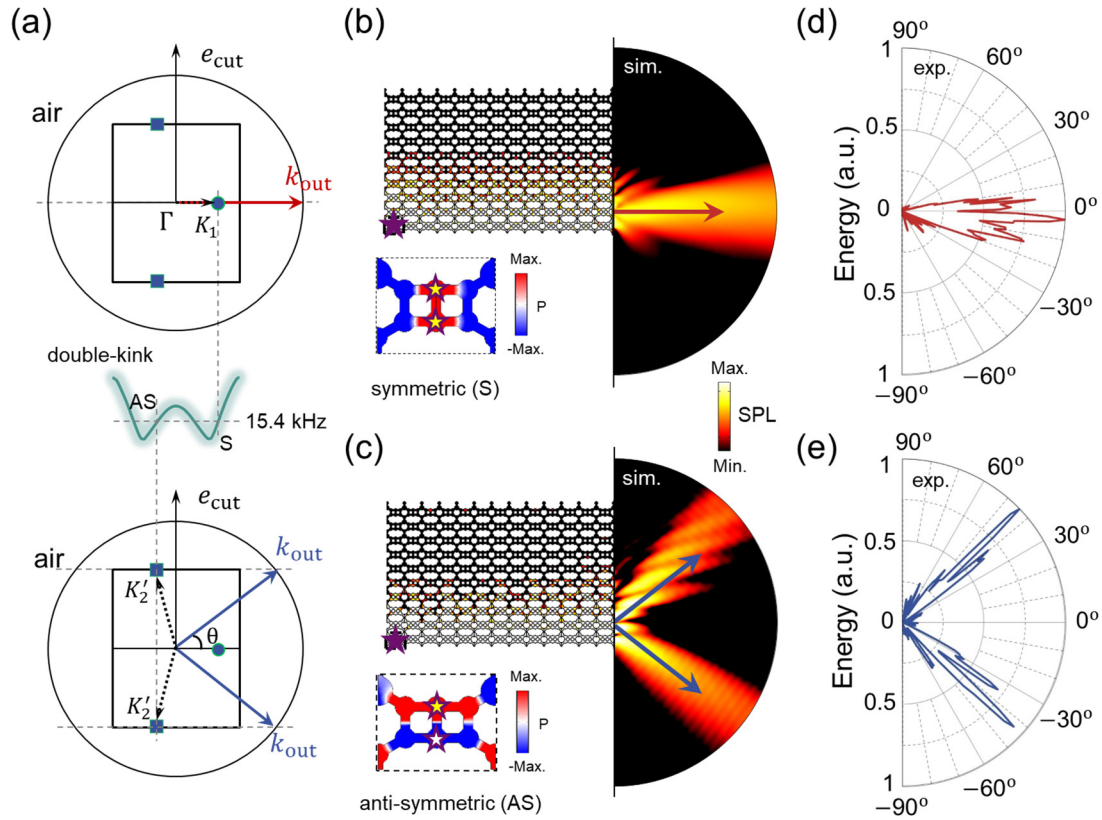

FIG. 4. Superdirectional sound radiation of double-kink valley states. (a) The k-space analysis, where the circle (rectangle) denotes the isofrequency line of air at 15.4 kHz (the first BZ). The e_{cut} denotes the direction of boundary cut. The dashed (solid) arrows represent the wave vectors in the S-graphene (radiation to air). (b), (c) Simulated field distributions of the sound-pressure level (SPL) excited by the two sources (star markers) with symmetric (S) and antisymmetric (AS) modes, respectively. The insets show the sound-pressure (P) distribution of a unit cell. (d), (e) Experimentally measured far-field radiation patterns detected on a semicircle with a radius of 21 cm away at 1° steps.

allowed, resulting in superdirectional sound radiation along the x axis. The situation is quite different for the AS branch since the K_2' valley has two equivalent Bloch wave vectors $k_y = \pm\pi/a_y$ at the BZ boundary. Therefore, we can obtain two oblique radiation beams. The refraction angles satisfy

$$\theta = \arcsin(k_y/k_0), \tag{3}$$

where k_0 represents the sound-wave vector in the air. The theoretical angles of the splitting refraction are $\pm 38.5^\circ$.

Thus, we are able to selectively generate normal radiation or oblique biradiation by exciting either the symmetric or antisymmetric mode of the double-kink state. Here, we set up two loudspeakers as sources. Only adjusting their phase difference (0 or π) can achieve regulation without changing any other configuration. As simulated results shown in Figs. 4(b) and 4(c), the radiation beams show superdirectional behavior due to the valley-locked and valley-dependent characters. The experimentally measured results in Figs. 4(d) and 4(e) agree well with the analysis and simulations (see Appendix I). The outgoing beam detected in the far field (21 cm away) is approximately $-2^\circ \pm 10^\circ$ wide for normal radiation and $\pm 41^\circ \pm 6^\circ$ wide for oblique biradiation. Hence, this design allows us to selectively excite the collimated outcoupling of the valley edge states that we can receive from a fixed direction, and vice versa. Additionally, the robustness of the valley state allows for the possibility of exciting superdirectional radiation even in the presence of defects (see Appendix J).

III. DISCUSSION AND OUTLOOK

The superdirectional outcoupling waves with the y-cut boundary, similar to that in conventional graphene systems [29,45], are related to the valley DOF. Furthermore, the AS-branch biradiation, which is absent in the single-kink case, could behave as bipositive or binegative refractions [46], other than the splitting fashion in Fig. 4. Additionally, more superdirectional radiation beams are possible in the case of more valleys [28,47]. Our study has several superior aspects and numerous properties that can be further explored. For example, the double-kink valley state can be self-guiding [44] on various boundary conditions, which is helpful for compact devices. By adjusting the position and phase of the excitation sources, the valley state can be excited to produce nearly unidirectional superdirectional acoustic radiation (see Appendix K). Since the two pairs of DPs can be manipulated independently [37], one can simply split one pair while keeping the other degenerate to study the coexistence of edge arcs and valley states. Constructing bilayer [30] or spin-valley coupled states [31] using multivalley acoustic crystals can further increase the DOF of manipulation.

In summary, we experimentally investigate the bulk-boundary correspondence for edge arcs in S-graphene acoustic crystals with multiple pairs of bulk DPs. All the edge arcs are related to the DPs, while their connection fashion is tunable. Both intrapair and interpair connections are allowed, depending on the boundary conditions. After opening a band gap, we observe *W*-type and *M*-type double-kink valley states, which can be utilized to develop directional yet tunable topological antennas. This work extends valley DOF and may provide a way to study the topological behavior of various other allotropes of the graphene structure [36] via acoustic crystals. The demonstrated Dirac physics associated with multivalleys constitutes a step towards high-capacity on-chip topological acoustic circuits [48]. Furthermore, the selectively superdirectional radiations based on double-kink states may help to improve and develop the functions of valleytronic devices.

ACKNOWLEDGMENTS

The work was jointly supported by the National Key R&D Program of China (Grants No. 2022YFA1404302 and No. 2022YFA1404404) and the National Natural Science Foundation of China (Grants No. 52022038, No. 92263207, No. 52103341, No. 11890700, No. 52027803, and No. 51721001).

APPENDIX A: THEORETICAL MODEL

The tight-binding approach (TBA) is an important method for predicting graphene properties from theoretical calculations. It is sufficient to use the nearest-neighbor (NN) TBA to simulate the band structure of *S*-graphene. We construct a TBA lattice model for the *S*-graphene acoustic crystal, as shown in Fig. 5(a). The unit cell contains eight atoms. The primitive lattice vectors are $\boldsymbol{a}_1 = [(2+\sqrt{3})a,\ 0]$, $\boldsymbol{a}_2 = (0,\ 3a)$, where we set the distance between two atoms $a = 1$ in the following. For simplicity, only the NN hopping with hopping strength t_0 is considered. Here, we set the onsite energy of atoms all zero. Based on lattice sites, the Hamiltonian is

$$H(k) = \begin{bmatrix} 0 & h_{12} & 0 & h_{14} & 0 & h_{16} & 0 & 0 \\ h_{12}^* & 0 & h_{23} & 0 & 0 & 0 & h_{27} & 0 \\ 0 & h_{23}^* & 0 & h_{34} & 0 & 0 & 0 & h_{38} \\ h_{14}^* & 0 & h_{34}^* & 0 & h_{45} & 0 & 0 & 0 \\ 0 & 0 & 0 & h_{45}^* & 0 & h_{56} & 0 & h_{58} \\ h_{16}^* & 0 & 0 & 0 & h_{56}^* & 0 & h_{67} & 0 \\ 0 & h_{27}^* & 0 & 0 & 0 & h_{67}^* & 0 & h_{78} \\ 0 & 0 & h_{38}^* & 0 & h_{58}^* & 0 & h_{78}^* & 0 \end{bmatrix}, \tag{A1}$$

with $h_{12} = t_0 e^{-\frac{i\sqrt{3}k_x a}{2} + ik_y a/2}$, $h_{14} = h_{56} = t_0 e^{-ik_y a}$, $h_{16} = h_{34} = t_0 e^{\frac{i\sqrt{3}k_x a}{2} + ik_y a/2}$, $h_{23} = h_{78} = t_0 e^{ik_y a}$, $h_{27} = h_{38} = t_0 e^{-ik_x a}$, $h_{45} = t_0 e^{\frac{i\sqrt{3}k_x a}{2} - ik_y a/2}$, and $h_{58} = h_{67} = t_0 e^{ik_x a}$. The energy spectrum can be obtained by diagonalizing the above Hamiltonian. As shown in Fig. 5(b), we numerically plot the bulk structure along high-symmetry points with hopping strength $t_0 = 1$, and we can see two Dirac points K_1 and K_2 along ΓX and MY, respectively. The $K_1/K_1^{'}$ DP comes from the crossing of the fourth and fifth bands, while the $K_2/K_2^{'}$ is of the third and sixth bands (red lines) in our model. Here, the two DPs are at the same energy, which is a little different from the results calculated by the acoustic model. It is because only NN hopping is considered in TBA.

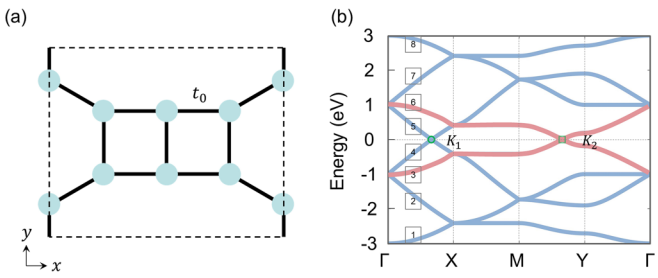

FIG. 5. Band structures of the *S*-graphene based on the tight-binding model. (a) The structure of the unit cell. Only the nearest-neighbor hoppings are considered and their strengths are the same ($t_0 = 1$). (b) The calculated bulk-band structures from the tight-binding model along high-symmetry directions. The third and sixth bands are marked by red lines. The green circular (rectangular) marker denotes the K_1 (K_2) Dirac point.

APPENDIX B: METHOD FOR CALCULATING THE RELATIVE BERRY PHASE

We have developed a computational method to study bulk-boundary correspondence from a topological invariant perspective, which can verify the existence of edge arcs in noncentrosymmetric unit cells. Unlike the conventional calculation method for the Berry phase that uses centrosymmetric unit cells, we employ a unique unit cell (black-dashed rectangular) with zigzag or bearded morphology at the lower boundary, as shown in Figs. 6(a) and 6(d), to accommodate our tuned boundaries. The Berry phase,

$$\phi_n = \oint A_n(\boldsymbol{k}) \cdot d\boldsymbol{k}, \tag{B1}$$

is a closed-path integral over the Berry connection:

$$A_n(\boldsymbol{k}) = i\langle u_{n,k}|\nabla_k|u_{n,k}\rangle, \tag{B2}$$

where n is the energy band index, and $u_{n,k}$ is the periodic function. Then, we discretize its first BZ into a regular mesh in k space with a grid size of 21×21 points. Here, we use the method of Wilson loop to calculate the Berry phases for every fixed k_x, and a more easily calculated formula is obtained:

$$\Phi(k_i) = -\mathrm{Im}\left\{\log\left[\det\left(\prod_{k_j} S_{(k_i,k_j),(k_i,k_{j+1})}\right)\right]\right\},$$
$$i,\ j = 1, \ldots 21, \tag{B3}$$

where S is an $(n \times n)$ overlap matrix, with $S^{lm} = \langle u^l_{(k_i,k_j)}|u^m_{(k_i,k_{j+1})}\rangle$, $l, m = 1, \ldots n$. There are eight bands in this unit cell; we calculate the four bands ($n = 4$) below the DPs for every fixed k_x. The results are shown in Figs. 6(b) and 6(e) from different unit cells, respectively. The values of the calculated Berry phase can be divided into two categories, i.e., values Φ_1 between the projection of the same Dirac pair

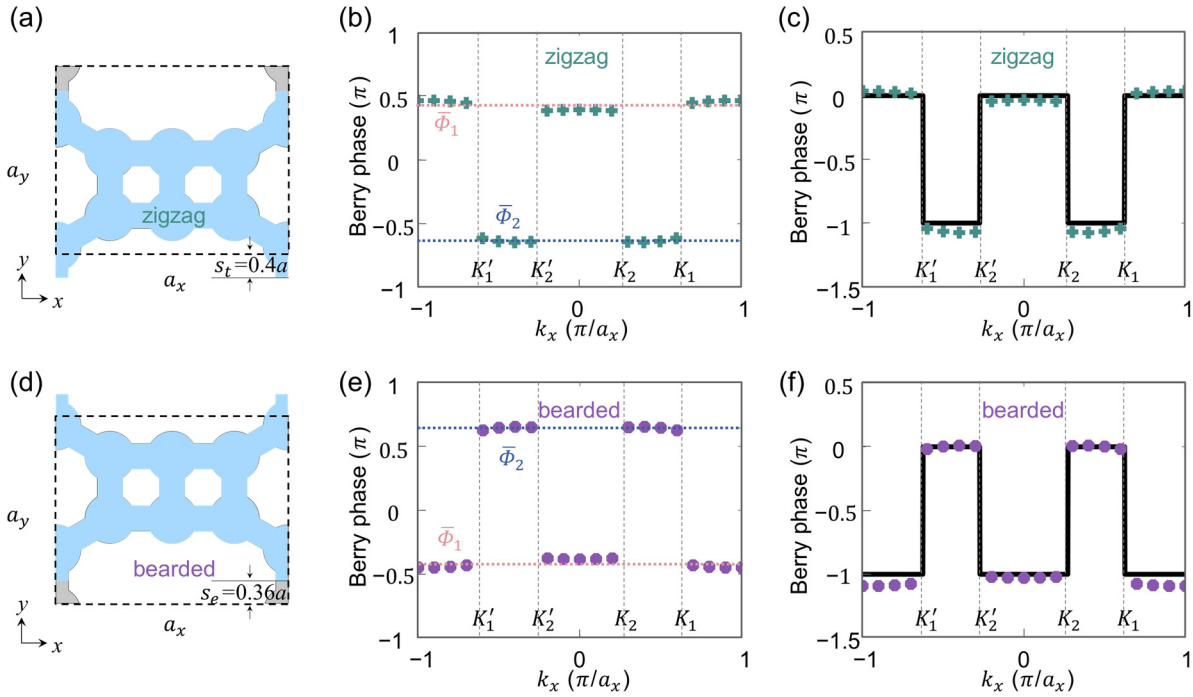

FIG. 6. Berry phases of the edge arcs. (a), (d) The unit cell (black-dashed rectangular) used for the calculation of the Berry phase with a zigzag boundary (truncated length $s_t = 0.4a$) and bearded boundary (elongated length $s_e = 0.36a$), respectively. (b), (e) Finite-element method simulation results of Berry phases for the zigzag (cyan dots) and bearded (purple dots) boundaries, respectively. The calculated results are divided into two categories, i.e., value Φ_1 for intrapair connections ($K_1 - K_1'$ and equivalent $K_2 - K_2'$) and Φ_2 for interpair connections ($K_1 - K_2$ and equivalent $K_1' - K_2'$), with the red and blue dashed lines representing their average values, respectively. (c), (f) The relative Berry phases changed from the values of the left panel, respectively.

($K_1 - K_1'$ and equivalent $K_2 - K_2'$) and Φ_2 between the projection of different Dirac pair ($K_1 - K_2$ and equivalent $K_1' - K_2'$), and their difference satisfies

$$|\Phi_1 - \Phi_2| \approx \pi. \tag{B4}$$

It is worth noting that the original calculated values are not exactly equal to the standard values 0 or $-\pi$, but rather some intermediate values, due to the truncated boundary cut into the atoms. However, as shown in Figs. 6(c) and 6(f), these values can be shifted down to approximately meet the standard values. We refer to these shifted values as the relative Berry phase:

$$\Phi^r = \Phi - \bar{\Phi}_v, \tag{B5}$$

where $v = 1$ or 2, and $\bar{\Phi}_v$ represents the average value (dashed color line). In the case of the zigzag-boundary case, we uniformly subtract $\bar{\Phi}_1$ to obtain the relative Berry phase as we show in Fig. 6(c), where the values between the projection of different Dirac pairs are close to $-\pi$, corresponding to the edge arcs of interpair connections. For the bearded boundary, we uniformly subtract $\bar{\Phi}_2$.

APPENDIX C: THE EVOLUTION OF THE EDGE STATES WHEN THE BOUNDARY MORPHOLOGY CHANGES

As shown in Fig. 7, we systematically investigate the evolution of edge states by adjusting the boundary with a continuous variation.

APPENDIX D: THE BERRY CURVATURE NEAR THE BZ CENTER

Figure 8(b) shows the Berry curvatures of the third band in the first BZ, which has the opposite values in the BZ center with the fourth band.

APPENDIX E: THE FIELD DISTRIBUTIONS OF THE VORTEX STATES

The field distribution of vortex states can be seen in Fig. 9.

APPENDIX F: THE EXPERIMENTAL SAMPLE OF THE VALLEY STATES

The experimental sample of the valley states is shown in Fig. 10.

APPENDIX G: THE PROJECTIVE BANDS WITH VARYING CAVITY RADIUS

As shown in the projected bands of Fig. 11, the self-guiding valley states can be achieved by changing the radius of only one circular cavity in the unit cell, and the size of its band gap can be adjusted accordingly.

APPENDIX H: THE POSITIVELY EXCITED MODES OF THE *W*-TYPE VALLEY STATE

The sound pressure distributions of the two modes excited along the $+x$ axis in the projected band are shown in Fig. 12.

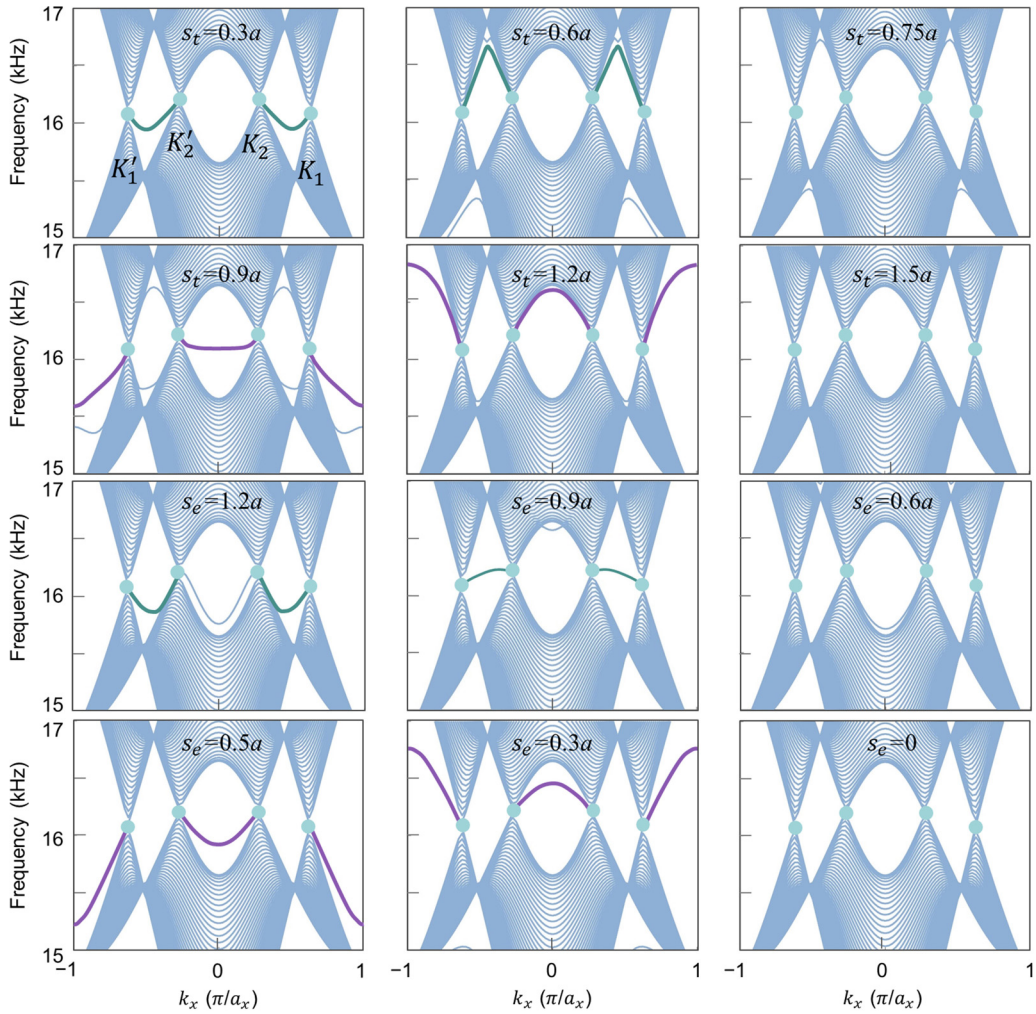

FIG. 7. The evolution of edge states adjusting the boundary with a continuous variation of the shear length (s) from 0 to $3a$ in the y direction. For shear lengths in the range $0 < s < 1.5a$, denoted as s_t for truncated length, the morphology of the edge states undergoes a gradual shift, resulting in a transition from interpair connections ($K_1 - K_2$ and equivalent $K_1' - K_2'$) to intrapair connections ($K_1 - K_1'$ and equivalent $K_2 - K_2'$) as s_t increases. The different connections are indicated by cyan and purple lines, respectively, and the transition occurs near the value $s_t = 0.75a$. When the truncated length is equal to $1.5a$, no edge states are observed. In the range where $1.5a < s < 3a$, which can be regarded as an elongated length s_e ($s_e = 3a - s$), the edge states exhibit a similar upward shift and transition in their connections as s_e decreases. An edge state connecting $K_2 - K_2'$ appears when $s_e = 1.2a$, but as s_e decreases, this edge state shifts upwards and is not part of the connection between the Dirac points, as observed at $s_e = 0.9a$. This state we consider to be a Tamm state, which is trivial and does not require further attention. During this process, certain edge states resembling Tamm states emerge. However, these states are not relevant to the two connection modes of interest and will not be subjected to further analysis. In summary, in our system, the boundary states exhibit only these two Dirac connections at different shear boundaries.

APPENDIX I: METHODS

1. Simulation methods

The simulations performed on the bulk bands, projected bands, and sound pressure are calculated by the software COMSOL. To calculate the bulk bands, we create the unit cell that has periodic boundary conditions in the x and y directions. We compute along the high-symmetric direction of the BZ to obtain our bulk-band diagrams. For calculating the projected bands, we construct the supercell with a y-direction period of 41 (21) in projecting the Dirac (valley) system, which established hard boundaries in the y direction and periodic boundaries in the x direction. To compute the sound pressure, we periodically arrange the unit cell for 13 and 10 in the x and y directions, respectively, and construct the bearded boundary and zigzag boundary with hard-boundary conditions in the upper and lower boundaries, respectively. By setting two-point sources at the position of the inset stars, as shown in Fig. 4(b), and adjusting their phase difference, different modes could be excited at 15.4 kHz.

2. Experimental methods

To excite the valley-state modes, we position the two sound sources in the cavities symmetrically located around the center of the unit cell, as depicted in the inset of Fig. 4(b). Both sources emit sound waves with identical frequency and amplitude. To achieve the excitation of different modes, the

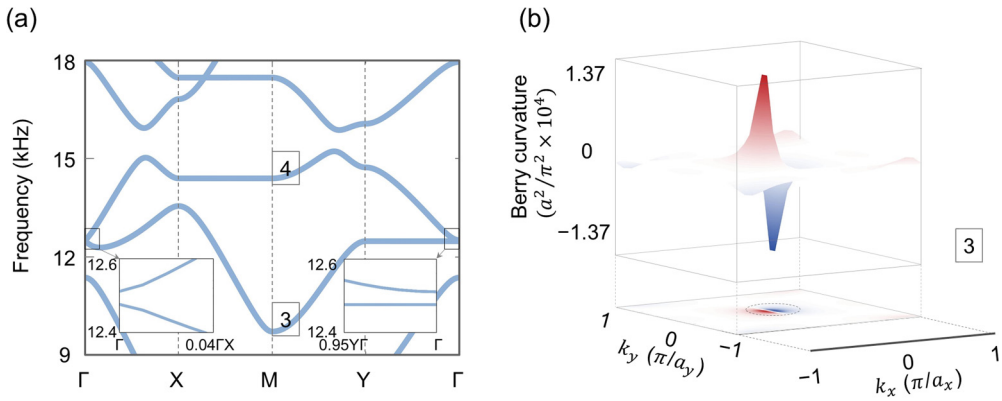

FIG. 8. The Berry curvature near the center of BZ. (a) The bulk structures from the third to fifth bands under the broken symmetry. (b) The calculated Berry curvatures of the third band in the first BZ. The nonzero Berry curvatures in the black-dashed circle region originate from the split of the degenerate point of the third and fourth bands near the Γ point. Opposite Berry curvatures are observed in this region of the fourth band. Since it does not affect the four valleys, this region has been omitted in the main text [Fig. 3(b)] to focus on our study.

only variation introduced is the phase difference between the two sources. For the measurements, we record the acoustic amplitudes at 1° intervals along a semicircle of radius 21 cm centered on the point of emission. The recorded values then are squared and normalized to produce the experimental data presented in Fig. 4.

APPENDIX J: THE ROBUSTNESS OF VALLEY STATES

As shown in Fig. 13, the double-kink valley state is still robustly transmitted in acoustic crystals as it passes through defect boundaries, such as deformation and cavity, and the superdirectional sound radiation can still be selectively exciting by adjusting the phase difference. The deformation is achieved by increasing the radius of the three adjacent air cavities on the boundary from $0.33a$ to $0.47a$, as depicted in Fig. 13(b). We construct the cavity by subtracting the structure inside the dashed circle (radius $0.47a$) of the boundary as shown in Fig. 13(d). The transmission spectra are obtained by positioning a source at the position of the asterisks, as shown in Figs. 13(c) and 13(e), and placing a probe 7 unit cells away from the source. From the transmission spectra and the acoustic radiation at the frequency of 15.4 kHz, we observe that in the defect cases of deformation, the edge states are still robust, and selective directional radiation can still occur by modulating the phase difference of the two-point sources. In the cavity case, it can be found that the transmission drops at the lower side of the working frequency because of the destruction of the original unit cell and the band-side effect. However, the robust sound transport generally works against moderate defects, which is similar to the conventional valley case.

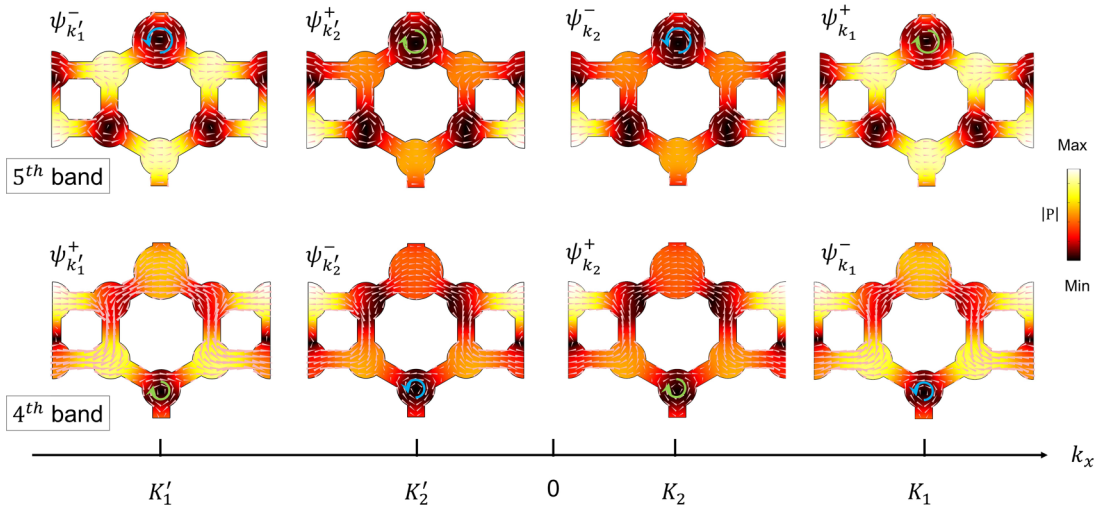

FIG. 9. The absolute values of sound pressure $|P|$ (color scale) distribution of the vortex states. To enhance the visibility of the vortex, we shifted the unit cell by half a period in the x direction. Once the degeneracy of the Dirac points was lifted, the field distributions of the local extremum of the fourth and fifth bands were observed along the horizontal coordinate (k_x). The light-pink arrows denote the direction of the energy flow. The states on the fifth band and fourth bands have opposite field distributions and different vortex directions, respectively. To indicate clockwise (green arrow) or anticlockwise (blue arrow) rotated vortices on the above and below cavities, we use the sign ±. It is important to note that the different Dirac point pairs have opposite signs and chirality, which is consistent with the Berry curvature that we calculated.

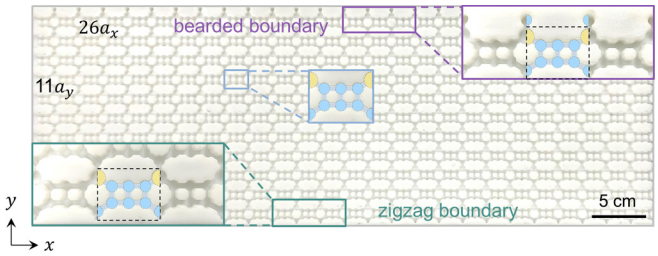

FIG. 10. Picture of the acoustic sample of the double-kink valley states with 26 × 11 periods. The insets in the figure show a zoomed-in view of the unit cell (blue rectangle), zigzag boundary (cyan rectangle), and bearded boundary (purple rectangle) with elongated cavity length. Both upper and lower boundaries are hard boundaries. Our samples are fabricated by 3D printing with photopolymer materials (geometry tolerance of 0.1 mm), which have a mass density of 1.16 g/cm^3, and can be modeled as hard-boundary conditions for air, due to the huge mismatch of acoustic impedance. The material properties remain constant over the laboratory temperature range. During the actual measurements, we use an acrylic plate of 1300 mm × 500 mm × 10 mm proportions to blanket the surface of the sample, thereby ensuring hard-boundary conditions in the z direction. We employ a commercial loudspeaker (AMT-47) to generate sound and a commercial probe (BSWA-MPA436A) to scan the pressure fields. The gathered amplitude and phase information of 25 periodic cavities can then be analyzed with NI cDAQ-9185 (NI 9250 & NI9260).

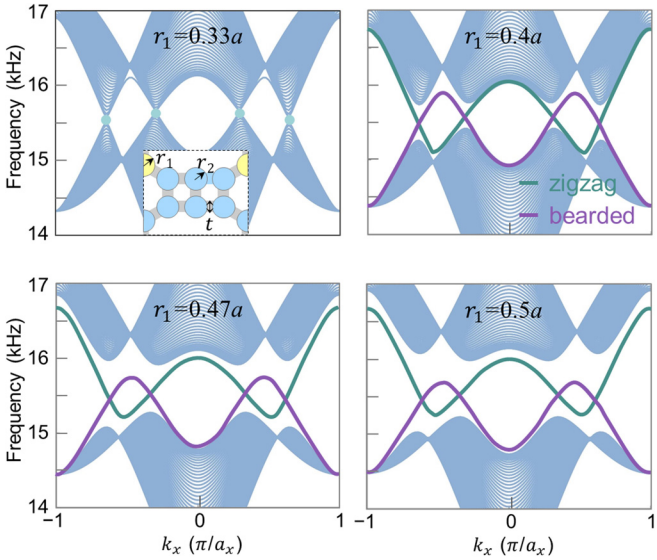

FIG. 11. The projected bands when gradually changing the radius of one of the cavities in the unit cell from 0.33a to 0.5a. As shown in the inset, the cavity marked in yellow is the one with a changed radius, and the radius of the blue cavity ($r_2 = 0.33a$) and the width of the coupling tube ($t = 0.3a$) remain constant. When the radius of the changed cavity $r_1 = r_2 = 0.33a$, the degeneracy of Dirac points is preserved, and a Tamm state appears on the bearded boundary. When $r_1 = 0.4a$, Dirac points are opened by breaking the spatial-inversion symmetry, at which time W-type and M-type double-kink valley states appear at the zigzag and bearded boundaries, respectively. As r_1 continues to increase, the band gap becomes larger, and the valley states correspond to moving away from the bulk band. When $r_1 = 0.47a$, which is the case for the projected bands calculated in our main text, the band gap is opened up more with $r_1 = 0.5a$, and there still are valley states.

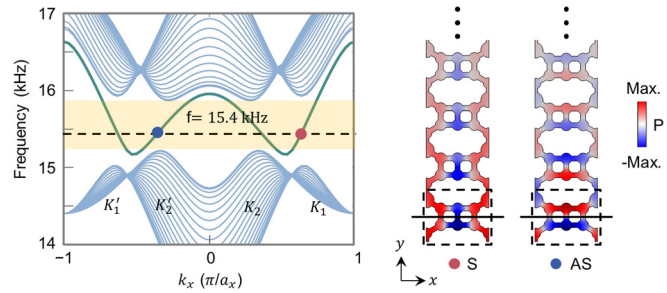

FIG. 12. The projected band structures of the W-type valley state. At a frequency of 15.4 kHz (indicated by the black-dashed line) and in the forward propagation direction of the $+x$ axis, there exist two branches (marked by red and blue dots) with positive group velocities corresponding to the K_1 and K_2' valleys, respectively. The sound-pressure (P) distributions of these branches differ; specifically, the red state is symmetrical (labeled as S) with respect to the central line along the x direction of the unit cell (indicated by the dashed black box), while the blue state is antisymmetric (labeled as AS).

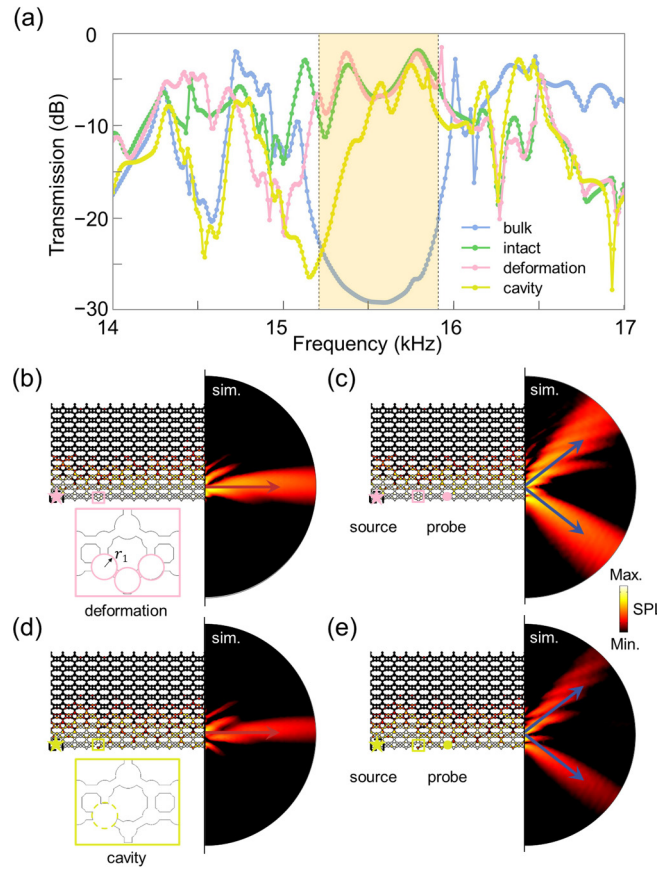

FIG. 13. The simulated transmission spectra and superdirectional sound radiation of double-kink valley states under deformation and cavity defects. (a) Transmission spectra. (b), (c) Simulated field distributions of SPL excited by two sources under the deformation boundary at 15.4 kHz. The inset (rectangle) shows a magnified structure of deformation ($r_1 = 0.47a$). (d), (e) Simulated field distributions of SPL excited by two sources under cavity boundary at 15.4 kHz. The dashed circle in the inset shows one removed site with a radius of 0.47a. The asterisks and dots denote the positions of the source and probe, respectively.

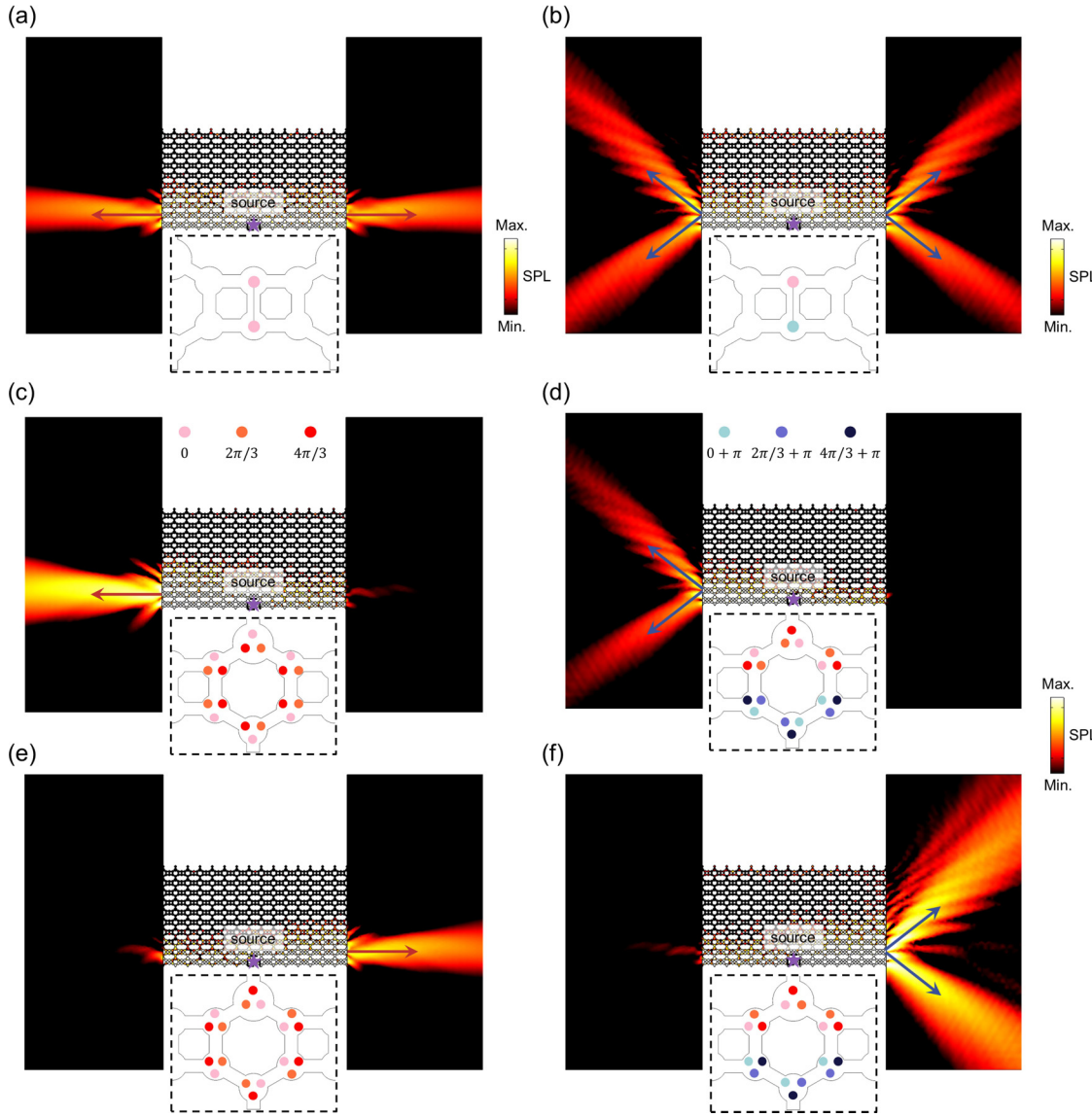

FIG. 14. The simulated field distributions for superdirectional radiation at a frequency of 15.4 kHz. (a), (b) Bidirectional normal (oblique) radiation excited by two-point sources with 0 (π) phase delay as shown in insets. (c), (e) Nearly unidirectional normal radiation excited by six sets of triangular arranged three-point sources in one unit cell. The phase difference of each set between adjacent point sources is $2\pi/3$, denoted as different colored dots (insets). The source phases of the upper and lower three sets exhibit mirror symmetry. (d), (f) Nearly unidirectional oblique biradiation case. By manipulating the positions and phases of the sources, both the direction and angle of the radiation are tunable, enabling the nearly unidirectional excitation of modes from different valleys on the boundary. Following this trend, 100% unidirectional transmissions can be achieved in principle.

APPENDIX K: THE NEARLY UNIDIRECTIONAL EXCITATION OF SUPERDIRECTIONAL RADIATION

The field distributions and emission efficiency for nearly unidirectional radiation can be seen in Fig. 14 and Table I, respectively.

TABLE I. The calculated emission efficiency (ratios between the energies outgoing from different boundaries and the sum of the two boundaries) from Fig. 14.

Fig.	14(a)	14(b)	14(c)	14(d)	14(e)	14(f)
Left boundary	50%	50.3%	92.6%	93.4%	14.2%	4.6%
Right boundary	50%	49.7%	7.4%	6.6%	85.8%	95.4%

[1] O. Klein, Die Reflexion von Elektronen an einem Potentialsprung nach der relativistischen Dynamik von Dirac, Z. Phys. **53**, 157 (1929).

[2] E. Schrödinger, Über die kräftefreie Bewegung in der relativistischen Quantenmechanik, Sitz. Preuss. Akad. Wiss. Phys. **24**, 418 (1930).

[3] X. Jiang, C. Shi, Z. Li, S. Wang, Y. Wang, S. Yang, S. G. Louie, and X. Zhang, Direct observation of Klein tunneling in phononic crystals, Science **370**, 1447 (2020).

[4] X. Zhang, Observing Zitterbewegung for photons near the Dirac point of a two-dimensional photonic crystal, Phys. Rev. Lett. **100**, 113903 (2008).

[5] S.-Y. Yu, X.-C. Sun, X. Ni, Q. Wang, X.-J. Yan, C. He, X.-P. Liu, L. Feng, M.-H. Lu, and Y.-F. Chen, Surface phononic graphene, Nat. Mater. **15**, 1243 (2016).

[6] M. Kohmoto and Y. Hasegawa, Zero modes and edge states of the honeycomb lattice, Phys. Rev. B **76**, 205402 (2007).

[7] Y. Plotnik, M. C. Rechtsman, D. Song, M. Heinrich, J. M. Zeuner, S. Nolte, Y. Lumer, N. Malkova, J. Xu, A. Szameit, Z. Chen, and M. Segev, Observation of unconventional edge states in "photonic graphene," Nat. Mater. **13**, 57 (2014).

[8] C.-H. Xia, H.-S. Lai, X.-C. Sun, C. He, and Y.-F. Chen, Experimental demonstration of bulk-hinge correspondence in a three-dimensional topological Dirac acoustic crystal, Phys. Rev. Lett. **128**, 115701 (2022).

[9] Z. Wang, Y. Chong, J. D. Joannopoulos, and M. Soljacic, Observation of unidirectional backscattering-immune topological electromagnetic states, Nature (London) **461**, 772 (2009).

[10] R. Fleury, D. L. Sounas, C. F. Sieck, M. R. Haberman, and A. Alù, Sound isolation and giant linear nonreciprocity in a compact acoustic circulator, Science **343**, 516 (2014).

[11] X. Ni, C. He, X.-C. Sun, X.-P. Liu, M.-H. Lu, L. Feng, and Y.-F. Chen, Topologically protected one-way edge mode in networks of acoustic resonators with circulating air flow, New J. Phys. **17**, 053016 (2015).

[12] Z. Yang, F. Gao, X. Shi, X. Lin, Z. Gao, Y. Chong, and B. Zhang, Topological acoustics, Phys. Rev. Lett. **114**, 114301 (2015).

[13] K. F. Mak, K. L. McGill, J. Park, and P. L. McEuen, The valley Hall effect in MoS2 transistors, Science **344**, 1489 (2014).

[14] J. Lu, C. Qiu, M. Ke, and Z. Liu, Valley vortex states in sonic crystals, Phys. Rev. Lett. **116**, 093901 (2016).

[15] J. Lu, C. Qiu, L. Ye, X. Fan, M. Ke, F. Zhang, and Z. Liu, Observation of topological valley transport of sound in sonic crystals, Nat. Phys. **13**, 369 (2017).

[16] X. Wu, Y. Meng, J. Tian, Y. Huang, H. Xiang, D. Han, and W. Wen, Direct observation of valley-polarized topological edge states in designer surface plasmon crystals, Nat. Commun. **8**, 1304 (2017).

[17] A. B. Khanikaev, S. H. Mousavi, W.-K. Tse, M. Kargarian, A. H. MacDonald, and G. Shvets, Photonic topological insulators, Nat. Mater. **12**, 233 (2013).

[18] L.-H. Wu and X. Hu, Scheme for achieving a topological photonic crystal by using dielectric material, Phys. Rev. Lett. **114**, 223901 (2015).

[19] J. Mei, Z. Chen, and Y. Wu, Pseudo-time-reversal symmetry and topological edge states in two-dimensional acoustic crystals, Sci. Rep. **6**, 32752 (2016).

[20] C. He, X. Ni, H. Ge, X.-C. Sun, Y.-B. Chen, M.-H. Lu, X.-P. Liu, and Y.-F. Chen, Acoustic topological insulator and robust one-way sound transport, Nat. Phys. **12**, 1124 (2016).

[21] D. Xiao, W. Yao, and Q. Niu, Valley-contrasting physics in graphene: Magnetic moment and topological transport, Phys. Rev. Lett. **99**, 236809 (2007).

[22] G. W. Semenoff, V. Semenoff, and F. Zhou, Domain walls in gapped graphene, Phys. Rev. Lett. **101**, 087204 (2008).

[23] J. Noh, S. Huang, K. P. Chen, and M. C. Rechtsman, Observation of photonic topological valley Hall edge states, Phys. Rev. Lett. **120**, 063902 (2018).

[24] M. Wang, L. Ye, J. Christensen, and Z. Liu, Valley physics in non-Hermitian artificial acoustic boron nitride, Phys. Rev. Lett. **120**, 246601 (2018).

[25] J. R. Schaibley, H. Yu, G. Clark, P. Rivera, J. S. Ross, K. L. Seyler, W. Yao, and X. Xu, Valleytronics in 2D materials, Nat. Rev. Mater. **1**, 16055 (2016).

[26] A. Rycerz, J. Tworzydło, and C. W. J. Beenakker, Valley filter and valley valve in graphene, Nat. Phys. **3**, 172 (2007).

[27] J. Li, R.-X. Zhang, Z. Yin, J. Zhang, K. Watanabe, T. Taniguchi, C. Liu, and J. Zhu, A valley valve and electron beam splitter, Science **362**, 1149 (2018).

[28] F. Gao, H. Xue, Z. Yang, K. Lai, Y. Yu, X. Lin, Y. Chong, G. Shvets, and B. Zhang, Topologically protected refraction of robust kink states in valley photonic crystals, Nat. Phys. **14**, 140 (2017).

[29] Z. Zhang, Y. Tian, Y. Wang, S. Gao, Y. Cheng, X. Liu, and J. Christensen, Directional acoustic antennas based on valley-Hall topological insulators, Adv. Mater. **30**, 1803229 (2018).

[30] J. Lu, C. Qiu, W. Deng, X. Huang, F. Li, F. Zhang, S. Chen, and Z. Liu, Valley topological phases in bilayer sonic crystals, Phys. Rev. Lett. **120**, 116802 (2018).

[31] C. He, S.-Y. Yu, H. Ge, H. Wang, Y. Tian, H. Zhang, X. C. Sun, Y. B. Chen, J. Zhou, M.-H. Lu, and Y.-F. Chen, Three-dimensional topological acoustic crystals with pseudospin-valley coupled saddle surface states, Nat. Commun. **9**, 4555 (2018).

[32] S. A. Skirlo, L. Lu, and M. Soljacic, Multimode one-way waveguides of large Chern numbers, Phys. Rev. Lett. **113**, 113904 (2014).

[33] S. A. Skirlo, L. Lu, Y. Igarashi, Q. Yan, J. Joannopoulos, and M. Soljacic, Experimental observation of large Chern numbers in photonic crystals, Phys. Rev. Lett. **115**, 253901 (2015).

[34] S.-M. Huang, S.-Y. Xu, I. Belopolski, C.-C. Lee, G. Chang, T.-R. Chang, B. Wang, N. Alidoust, G. Bian, M. Neupane, D. Sanchez, H. Zheng, H. T. Jeng, A. Bansil, T. Neupert, H. Lin, and M. Z. Hasan, New type of Weyl semimetal with quadratic double Weyl fermions, Proc. Natl Acad. Sci. USA **113**, 1180 (2016).

[35] Q. Chen, F. Chen, Y. Pan, C. Cui, Q. Yan, L. Zhang, Z. Gao, S. A. Yang, Z. M. Yu, H. Chen, B. Zhang, and Y. Yang, Discovery of a maximally charged Weyl point, Nat. Commun. **13**, 7359 (2022).

[36] L.-C. Xu, R.-Z. Wang, M.-S. Miao, X.-L. Wei, Y.-P. Chen, H. Yan, W.-M. Lau, L.-M. Liu, and Y.-M. Ma, Two dimensional Dirac carbon allotropes from graphene, Nanoscale **6**, 1113 (2014).

[37] A. Bandyopadhyay, S. Datta, D. Jana, S. Nath, and M. M. Uddin, The topology and robustness of two Dirac cones in S-graphene: A tight binding approach, Sci. Rep. **10**, 2502 (2020).

[38] J. Tworzydlo, B. Trauzettel, M. Titov, A. Rycerz, and C. W. Beenakker, Sub-Poissonian shot noise in graphene, Phys. Rev. Lett. **96**, 246802 (2006).

[39] R. A. Sepkhanov, Y. B. Bazaliy, and C. W. J. Beenakker, Extremal transmission at the Dirac point of a photonic band structure, Phys. Rev. A **75**, 063813 (2007).

[40] M. Blanco de Paz, C. Devescovi, G. Giedke, J. J. Saenz, M. G. Vergniory, B. Bradlyn, D. Bercioux, and A. García-Etxarri, Tutorial: Computing topological invariants in 2D photonic crystals, Adv. Quantum Technol. **3**, 1900117 (2019).

[41] H.-X. Wang, G.-Y. Guo, and J.-H. Jiang, Band topology in classical waves: Wilson-loop approach to topological numbers and fragile topology, New J. Phys. **21**, 093029 (2019).

[42] W. Yao, S. A. Yang, and Q. Niu, Edge states in graphene: From gapped flat-band to gapless chiral modes, Phys. Rev. Lett. **102**, 096801 (2009).

[43] X. Xi, J. Ma, S. Wan, C.-H. Dong, and X. Sun, Observation of chiral edge states in gapped nanomechanical graphene, Sci. Adv. **7**, eabe1398 (2021).

[44] R. Xi, Q. Chen, Q. Yan, L. Zhang, F. Chen, Y. Li, H. Chen, and Y. Yang, Topological chiral edge states in deep-subwavelength valley photonic metamaterials, Laser Photonics Rev. **16**, 2200194 (2022).

[45] T. Ma and G. Shvets, All-Si valley-Hall photonic topological insulator, New J. Phys. **18**, 025012 (2016).

[46] M. H. Lu, C. Zhang, L. Feng, J. Zhao, Y. F. Chen, Y. W. Mao, J. Zi, Y. Y. Zhu, S. N. Zhu, and N. B. Ming, Negative birefraction of acoustic waves in a sonic crystal, Nat. Mater. **6**, 744 (2007).

[47] D. Jia, Y. Ge, H. Xue, S.-q. Yuan, H.-X. Sun, Y. Yang, X.-j. Liu, and B. Zhang, Topological refraction in dual-band valley sonic crystals, Phys. Rev. B **103**, 144309 (2021).

[48] M. Yan, J. Y. Lu, F. Li, W. Y. Deng, X. Q. Huang, J. H. Ma, and Z. Y. Liu, On-chip valley topological materials for elastic wave manipulation, Nat. Mater. **17**, 993 (2018).